Local scanning electrochemical microscopy analysis of a lithium-based conversion layer on AA2024-T3 at progressive stages of formation

Li, Ziyu; Li, Gaojie; Visser, Peter; Homborg, Axel; Gonzalez-Garcia, Yaiza; Mol, Arjan

DOI
10.1016/j.electacta.2023.143270

Publication date
2023

Document Version
Final published version

Published in
Electrochimica Acta

Electrochimica Acta 469 (2023) 143270

Contents lists available at ScienceDirect

Electrochimica Acta

journal homepage: www.journals.elsevier.com/electrochimica-acta

Local scanning electrochemical microscopy analysis of a lithium-based conversion layer on AA2024-T3 at progressive stages of formation

Ziyu Li [a,*], Gaojie Li [a], Peter Visser [b], Axel Homborg [a,c], Yaiza Gonzalez-Garcia [a], Arjan Mol [a]

[a] Department of Materials Science and Engineering, Delft University of Technology, Mekelweg 2, Delft 2628CD, the Netherlands
[b] AkzoNobel, Rijksstraatweg 31, Sassenheim, AJ 2171, the Netherlands
[c] Netherlands Defence Academy, Het Nieuwe Diep 8, Den Helder, AC 1781, the Netherlands

ARTICLE INFO

Keywords:
Aluminium alloy
Inhibitor
Lithium-based conversion layer
SECM

ABSTRACT

Scanning electrochemical microscopy (SECM) is employed to characterize the evolution of local electrochemical surface activity during lithium-based conversion layer formation on legacy aerospace aluminium alloy AA2024-T3. Initially, three types of studied intermetallic particles - S-, θ- and constituent phases - act as active cathodic areas. Subsequently, θ- and constituent phases show passivation preceding that of S-phase particles during the later conversion layer formation stages. The entire surface, including the matrix region, shows a higher reactivity at the beginning and then gradually shows decreasing reactivity. Hydrogen evolution-generated bubbles attach to the alloy surface and locally hinder the conversion layer formation, weakening the corrosion protection the conversion layer provides at those locations.

1. Introduction

The 2xxx and 7xxx series of heat-treatable wrought aluminium alloys, representing Al–Cu–(Mg) and Al–Zn–Mg(–Cu) systems, respectively, have been widely applied in high-performance structural aerospace and transportation applications owing to their high strength-to-weight ratio, good elastic stiffness, excellent ductility, modest price and very good manufacturability [1–4]. However, the lack of sufficient corrosion resistance in harsh environments due to the heterogeneous distribution of intermetallic particles (IMPs) restricts their practical use without pre-treatment [5,6] and active protective coatings [7,8]. In Al–Cu–Mg alloys, IMPs nominally include three broad particle classes: dispersoids, precipitates, including S-phase (Al_2CuMg) and θ-phase (Al_2Cu), and constituent particles [5,9]. Precipitates form during heating operations in the solid state due to variations in the alloying solid solubility with temperature and have an age hardening effect. Constituent phases are nominally >1 μm in size and have compositions often enriched in transition metals including Al, Mn, Fe, Cu and Si in various ratios. S-phase particles typically exhibit a higher electrochemical activity as compared to other IMPs [10]. Corrosion protective measures based on surface treatment and organic coating application have been widely implemented in industrial practice due to their cost effectiveness, versatility and relatively simple application process characteristics [11–13].

Lithium salts are considered a promising candidate within the range of environmentally friendly inhibitors loaded into organic coatings for the corrosion protection of aerospace aluminium alloys since 2010 [14–17]. Leached lithium salts have been shown to form a protective conversion layer at an artificial coating defect during neutral salt spray test (ASTM B-117) [16]. Early relevant studies date back to the 1980s when Gui et al. [18] generated a lithium-based conversion layer by applying anodic polarization on AA6061-T6 panels. Rangel et al. reported that such conversion layer is robust and remarkably resistant to chloride ion attack [19,20]. Subsequent research showed that lithium ions can gradually be intercalated into aluminium hydroxide when exposed to a highly alkaline liquid environment containing lithium salts, generating a stable protective film on aluminium alloy surfaces [20,21]. Further structural and compositional analysis carried out by Buchheit et al. showed that the generation of an Al-Li layered double hydroxide layer (LDH) contributed to the enhanced corrosion barrier performance [22,23]. Over the last decade, the lithium-based inhibitor coating technology has been well studied for both organic coating systems and conversion treatment of bare aluminium alloys, indicating that lithium salts might be a promising alternative for the replacement of Cr (VI)-containing inhibitor chemistries for structural aerospace applications [24–29].

* Corresponding author.
E-mail address: Z.Li-12@tudelft.nl (Z. Li).

https://doi.org/10.1016/j.electacta.2023.143270
Received 31 July 2023; Received in revised form 26 September 2023; Accepted 26 September 2023
Available online 27 September 2023

In prior studies, lithium-based conversion layers have been characterized by linear polarization resistance (LPR) and Electrochemical Impedance Spectroscopy (EIS) performed at discrete time frames to quantify their corrosion protective properties in an aggressive solution at short exposure times (ranging from hours to 7 days) [28,30,31]. The system must maintain a relatively stable dynamic equilibrium during the measurements to obtain reliable data. This condition might limit the detection of fast-kinetic electrochemical reactions and valuable information of the corrosion (inhibition) mechanism might be missed. This limitation can be overcome by applying electrochemical noise (EN) techniques. Instantaneous and continuous, i.e. time-resolved, information on corrosion (inhibition) processes can be obtained, also for metastable and fast-kinetic electrochemical systems [32,33]. Yet, without spatial resolution, EIS and EN can only provide electrochemical information generated over the complete exposed surface area. Aluminium alloys typically undergo localized corrosion processes when exposed to aggressive environments [2,34–36] and they are highly related to various types of intermetallic phases [5,6,37]. Therefore, a local electrochemical technique is needed to adequately reveal the local electrochemical differences with adequate lateral resolution. For that purpose, the scanning electrochemical microscopy (SECM) technique is considered a suitable method since it harvests spatially-resolved electrochemical information of a heterogeneous electroactive surface. This technique employs an ultramicroelectrode (UME) to probe and map the electrochemical activity of a local surface area of interest during exposure to an electrolyte [38]. SECM has been widely applied to evaluate the formation of inhibitor films on aluminium alloys [39], the heterogeneous electrochemical properties of aluminium alloys at IMP containing areas [40,41], and the electrochemical activity at an artificial coating defect in the absence or presence of inhibitors in the coating [42,43].

In the present work, SECM and EN techniques are applied to resolve the formation process of a lithium-based conversion layer spatiotemporally. Different stages during the conversion layer formation period are analysed to study the evolution of the surface electrochemical behaviour at a microscale level. Local areas, including IMPs and the adjacent aluminium matrix are compared to elucidate different stages of local formation during the growth of the lithium-based conversion layer.

2. Experimental

2.1. Materials and experimental set-up

All working electrodes originated from a commercial grade AA2024-T3 sheet with a thickness of 0.8 mm (Goodfellow, UK). Rectangular specimens with a size of 8 mm × 18 mm are produced. Two specimens are embedded in epoxy resin for EN measurements to prepare identical-electrode samples. A detailed description of sample fabrication and the electrochemical cell for the preparation of the conversion layer can be found in previously published work [32,33]. Samples are immersed in a static conversion bath (0.01 M Li_2CO_3 and 0.01 M NaCl) for seven different time durations (0 s, 60 s, 200 s, 700 s, 2000 s, 4000 s, 14,500 s) to prepare and study the conversion layers at different formation stages. Formed conversion layers are washed thoroughly using deionized water, dried using cool air, and left in a desiccator before subsequent SECM and EN measurements. The purpose of this step is to quench the conversion layer formation process. Laboratory-grade chemicals used in this work were ordered from Sigma-Aldrich (St. Louis, MO, USA).

For SECM samples, a cross-scribe is made on the conversion layers. This mark is used as a reference location so that both the SECM and scanning electron microscope/ energy dispersive X-ray (SEM/EDX) images can be matched. All specimens for SECM and EN are covered by a highly-impermeable sealing tape with an exposed round area of 4 mm diameter. Morphological information is obtained using a JEOL JSM-6500F field emission SEM using an acceleration voltage of 15 kV at a working distance of 25 mm. Backscattered electron images (BEI) and secondary electron images (SEI) are collected. The local chemical surface composition is analysed using EDX. A schematic representation of the sample processing sequence is shown in Fig. 1.

2.2. SECM instrumentation and experimental procedures

Scanning electrochemical microscopy (SECM) is executed using biologic Instruments SECM model M370. A Pt disk UME (10 μm in diameter), with an RG (radius of the insulating glass sheath divided by the radius of the Pt disk) of 5, was purchased from CH Instruments Inc. and served as working electrode. A saturated Ag/AgCl, KCl and a Pt thin plate are used as reference electrode (RE) and counter electrode (CE), respectively. In this work, all voltages are with respect to the Ag/AgCl reference electrode unless otherwise stated. The SECM setup and the detailed apparatus are shown in Fig. 2. In addition to the high spatial resolution, SECM is well-known for its versatility and various operation modes such as feedback mode to differentiate insulating or conducting areas or generation/collection mode to investigate the interaction between an electroactive surface and chemical species in the electrolyte [38,44]. In this paper, a borate buffer solution containing 2 mM FcMeOH serving as mediator is used for SECM and EN measurements. The borate buffer is prepared using 10 mM sodium tetraborate, and then adjusted to pH 7.4 with 0.5 M boric acid to maintain the stability of the alloy surfaces during the SECM measurements [41,45–47]. Feedback mode data collection is utilized based on the redox mediator FcMeOH [41].

Cyclic voltammetry (CV) measurements are conducted to verify the cleanliness of the probe electrode with the probe held several millimetres away from the surface before any SECM measurement. All current signals are normalized using the steady-state current obtained from the CV test (Fig. S1) for a better comparison amongst the various measurements. Before SECM measurements, the stage is levelled by measuring a negative feedback approach curve over the covering tape. SECM mapping in a constant height is obtained by scanning the tip in the x–y plane and recording the tip current simultaneously. The distance between the tip and substrate is adjusted to around 5 μm employing an approach curve. Each measurement was performed over a working area of 180 μm × 140 μm with a scanning speed of 10 μm/s. For approach curves, the tip is moved toward the substrate surface at a velocity of 10 μm/s (steps of 1 μm, waiting time of 0.1 s at each point). Before approaching, a quick mapping was performed so that local areas with relatively high current values were avoided to make sure that the approach curves were measured above the aluminium matrix. For both modes, the SECM tip is biased at a voltage of 0.5 V to oxidize FcMeOH while the substrate is maintained at open circuit potential (OCP) state. All experiments are performed at room temperature 22 ± 2 °C, in solution open to the air. Experiments were repeated at least twice to confirm reproducibility.

2.3. EN measurements and analysis

For EN experiments, a two-electrode configuration is selected in this work. One exposed area chosen on either of the two panels is adopted to monitor the potential noise signal. Electrical contact is established with a Cu adhesive tape connected to the working electrode. The reference electrode used for EN is identical to that applied for SECM. Potential values recorded here are with respect to this reference electrode unless mentioned otherwise. All EN measurements are performed under open circuit conditions. The volume of the solution for EN measurement is 1 mL each time. A Compactstat (Ivium Technologies) is employed to record potential signals. A Faradaic cage is used to place the Compactstat and the electrochemical cell to avoid interference from external electromagnetic sources. The sampling frequency is 20 Hz and a low-pass filter of 10 Hz was used to avoid aliasing. The EN data are analysed using Matlab from MathWorks. All EN tests were performed at least in triplicate.

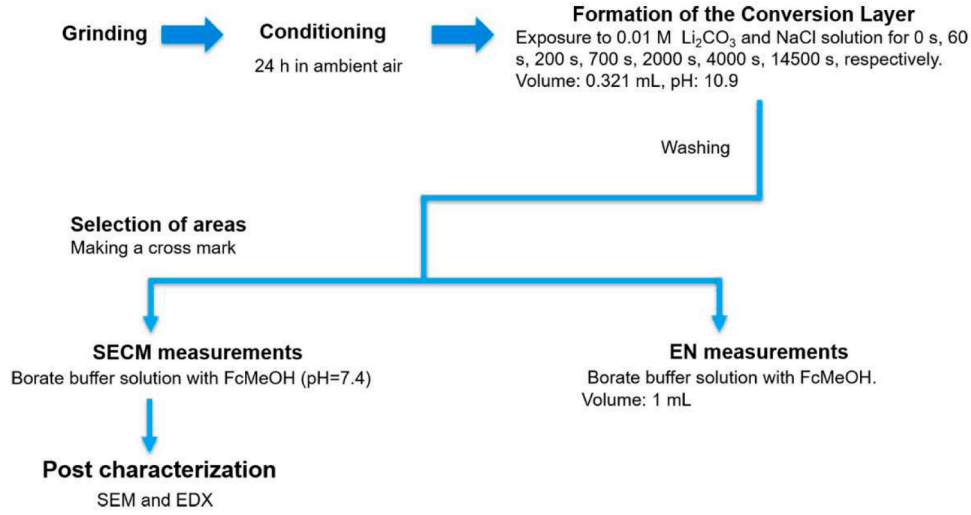

Fig. 1. Sequence diagram of the experimental procedure for the SECM, SEM and EN measurements.

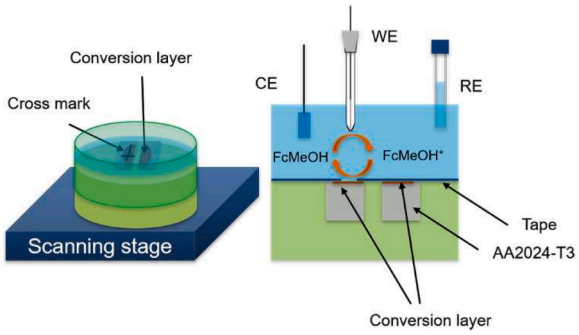

Fig. 2. Schematic illustration of SECM measurement.

In the EN noise, a DC component is inevitable due to the instability of the system and the changing outline of the electrode under corrosion attack. The DC component does not contain any useful information but generates false low frequencies and can interfere with the signal processing [48,49]. Therefore, the DC trend must be effectively removed but at the same time, useful data must be preserved as much as possible before data analysis. Previous researchers have proposed various strategies for trend removal, like moving average, polynomial and linear trend removal, wavelet analysis and empirical mode decomposition [48, 49]. In this work, a time-frequency trend removal is adopted using an eight-level discrete wavelet decomposition (DWT) with a Daubechies 4 wavelet. This method has already proven to be valid in our previous work [32,33]. After removing the DC component, an energy distribution plot (EDP) is applied to resolve the frequency range of the dominant energy contribution [50]. The time window from 4000 s to 6000 s is selected for analysis since this timeframe is within the SECM imaging period. Apart from around 30 min for levelling and locating the cross mark, SECM mapping lasts almost 90 min each time. The dominant energy contribution with certain time scales indicates the electrochemical reactions which contribute most to shape the outline of the EN signal. In this work, eight different time scales ranging from short, medium to long correspond to activation-, mixed-, and diffusion-controlled processes, respectively [48].

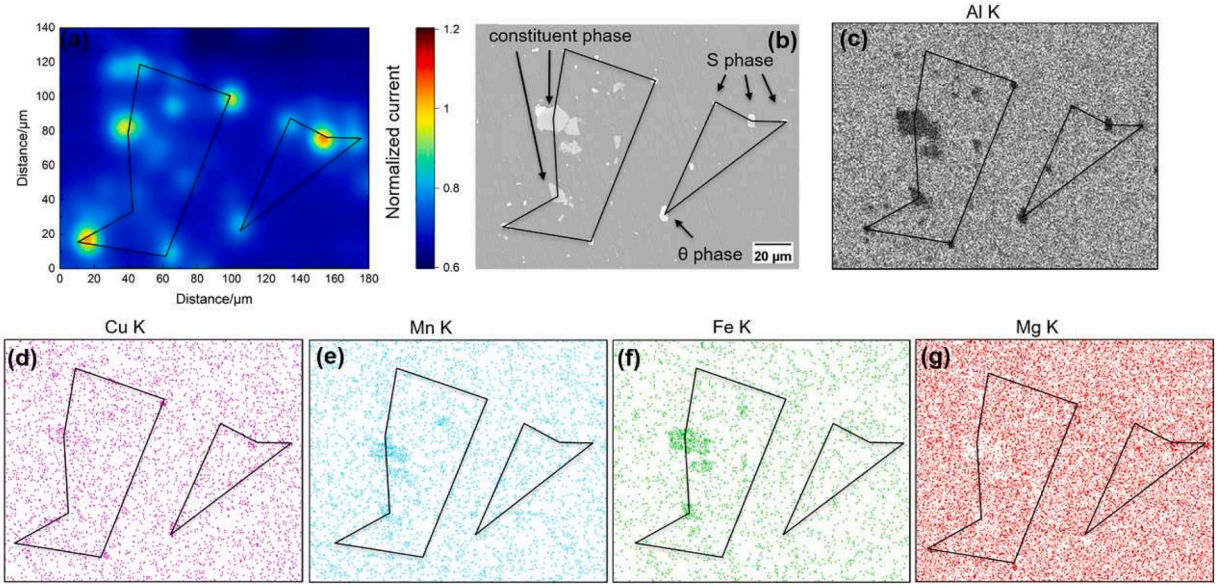

Fig. 3. SECM maps of AA2024-T3 without conversion treatment obtained in a borate buffer solution containing 2 mM FcMeOH (a) and corresponding BEI image (b), and EDX maps for Al (c), Cu (d), Mn (e), Fe (f), Mg (g).

3. Results and discussion

3.1. Early stages of the conversion layer growth

Fig. 3 shows SECM imaging and corresponding BEI/EDX characterization for the unexposed sample, i.e. before being immersed in the conversion bath (t = 0 s). Active areas in SECM mapping and corresponding IMPs are marked by black lines. FcMeOH is oxidized at the UME and then an enhanced current is obtained when the probe scans over an active region where $FcMeOH^+$ is reduced back to FcMeOH [41]. Although the native oxide protective layer remains stable under a relatively neutral liquid environment, it is insufficient to suppress local electrochemical reactions occurring at the surface. The "hot spot" regions observed in Fig. 3a are associated with the locations of different types of IMPs, as shown by SEM/EDX pictures in Fig. 3b-g. Enlarged images of several representative IMPs and their corresponding elemental compositions can be found in Fig. S2.

According to previous studies, the electrochemical interaction between the aluminium matrix and IMPs is driven by their dissimilar chemical compositions [40,41]. Previous work from our team has characterized the morphological evolution of S-, θ- and constituent phases, and the adjacent aluminium matrix at the AA2024-T3 surface during the formation process of a lithium-based conversion layer [51]. Herein, the variation of local electrochemical properties at and adjacent to IMPs is discussed. All S-, θ- and constituent phases form active sites for $FcMeOH^+$ reduction, meaning they all serve as cathodic areas when exposed to a borate buffer electrolyte. For the S-phase, it has been reported that anodic dealloying of the active elements Mg and Al occurs first and then the transition from anodic to cathodic region takes place due to Cu enrichment [6,34,35,37]. However, the S-phase acting as anodic zones is not observed in this work which may be due to the missing local electrochemical information of the S-phase immediately at the start [37] since levelling and locating the cross marks takes around 30 min before starting the SECM measurements. The presence of Mg shown in the EDX elemental composition maps of Figs. 3 g and S2 indicates that the buffer solution used in this work is relatively mild and non-corrosive compared to other solutions such as Na_2SO_4, where Mg was not detected on the AA2024-T3 after short immersion experiments [40]. In addition, many small IMPs with a submicron size are seen in Fig. 3b, but their electrochemical activity cannot be distinctly located in Fig. 3a due to the resolution limit in this work: IMPs only larger than 2 μm are analysed.

Fig. 4 presents the SECM mapping and relevant SEM/EDX results for samples with a lithium-based conversion layer formation time of 60 s corresponding to the lowest OCP during the immersion period [32]. It is clear that the averaged current in Fig. 4a rises drastically compared to that shown in Fig. 3a. This phenomenon indicates a more active state due to the dissolution of the native oxide film by the highly alkaline conversion bath solution (pH = 10.9). The S-, θ- and constituent phases still act as strong cathodic sites but present a wider "hot spot" area compared to that in Fig. 3a. Larger high current regions observed in Fig. 4a might be attributed to the faster dealloying of the S-phase in the aggressive conversion solution, leading to a larger redistributed-Cu area [51]. In addition, it is observed that the conducting activity is not uniform all over the aluminium matrix region. Regions far away from IMPs present a relatively lower reactivity which may be due to its lower alloying element content [4].

Fig. 5 reveals the SECM imaging and matched SEM/EDX for samples with a lithium-based conversion layer formation time of 200 s. The S-, θ- and constituent phases still behave as cathodic areas, albeit less significantly. The zoomed-in image of the θ-phase and its chemical composition on the left side of the mapped region is provided in Fig. S3. The averaged current in Fig. 5a is even higher than that shown in Fig. 4a although the OCP starts rising after 60 s duration in the conversion bath solution [32]. Furthermore, the current distribution becomes more homogeneous as compared to the results shown in Figs. 3a and 4a. The observation implies a decrease of the potential difference between IMPs and the aluminium matrix. For IMPs, the initial growth of the conversion layer over the S-phase and copper enrichment for *s*-, θ- and constituent phases shift the OCP towards less negative values [51]. Similarly, noble elements, particularly Cu, reside in the aluminium matrix. These gradually enrich the surface during the aluminium surface dissolution stage, which drives the OCP of the aluminium matrix to more noble values as well [52].

Fig. 6 shows the SECM mapping and corresponding BEI/EDX images for the sample with a lithium-based conversion layer formation time of 700 s. The current distribution shows a heterogeneous behaviour again but with a lower average current in total, especially owing to the current contribution from the aluminium matrix. The S-, θ- and constituent phases still act as strong cathodic locations. The transition of the aluminium matrix from an active towards a passive behaviour is attributed to the formation of the columnar top layer [32,51], although the corrosion protection is still insufficient to inhibit electron exchange reactions. The petal-like Li-Al LDH barrier protection is too limited to

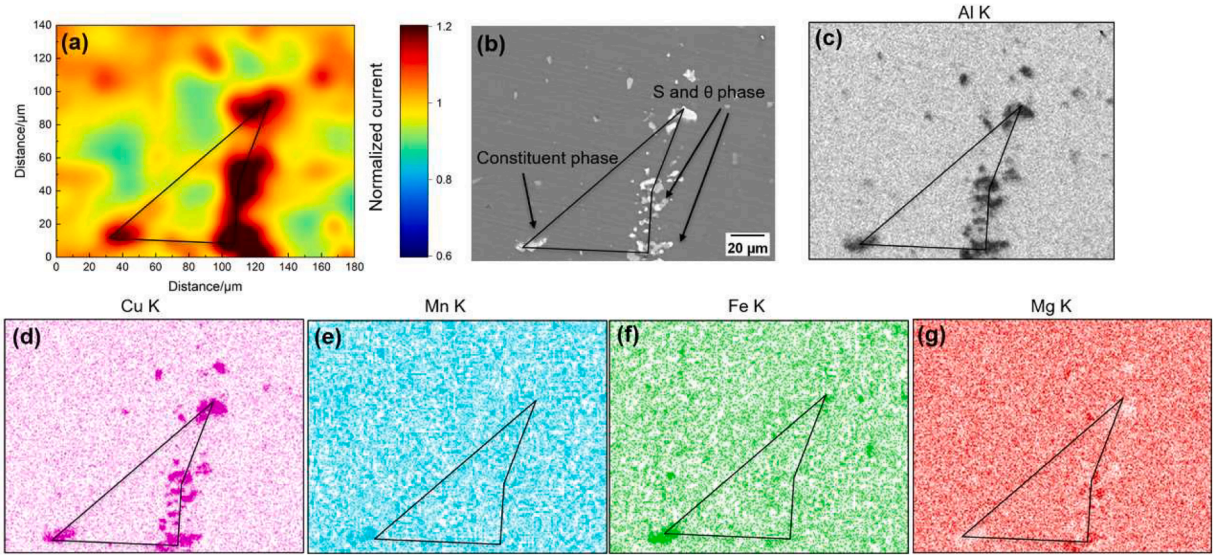

Fig. 4. SECM maps of AA2024-T3 immersed in the conversion bath for 60 s obtained in a borate buffer solution containing 2 mM FcMeOH (a) and corresponding BEI image (b), and EDX elemental maps for Al (c), Cu (d), Mn (e), Fe (f), Mg (g).

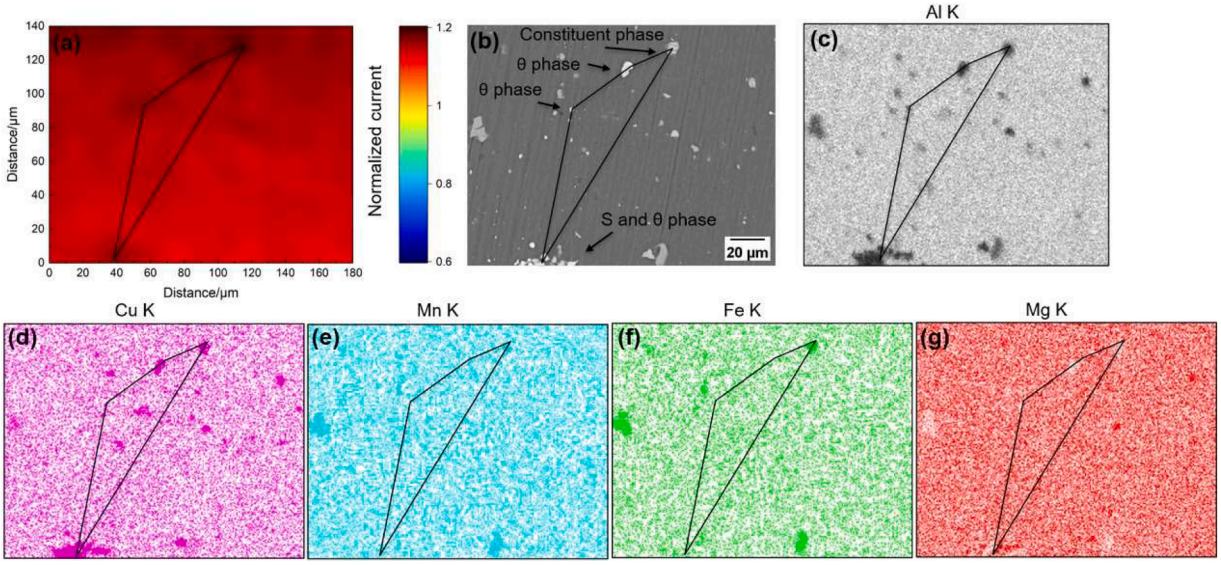

Fig. 5. SECM maps of AA2024-T3 immersed in the conversion bath for 200 s obtained in a borate buffer solution containing 2 mM FcMeOH (a) and corresponding BEI image (b), and EDX maps for Al (c), Cu (d), Mn (e), Fe (f), Mg (g).

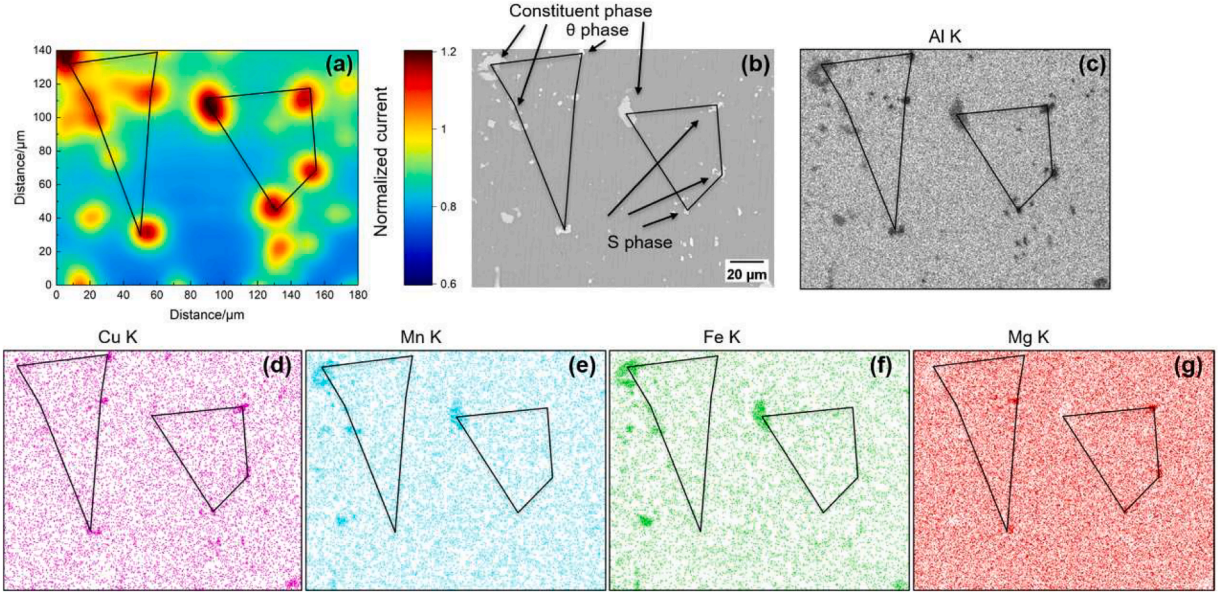

Fig. 6. SECM maps of AA2024-T3 immersed in the conversion bath for 700 s obtained at borate buffer solution containing 2 mM FcMeOH (a) and corresponding BEI image (b), and EDX maps for Al (c), Cu (d), Mn (e), Fe (f), Mg (g).

effectively suppress the diffusion of ionic species between the alloy surface and electrolyte [32,51]. For the IMPs, the S-phase shows an insignificant growth of the conversion layer and a more severe dealloying, leading to a higher surface enrichment of noble elements [51]. Although θ- and constituent phases are electrochemically relatively stable compared to the S-phase, the absence of a protective conversion layer at this formation stage and, hence, further dealloying render these to act as cathodic regions as well [51].

It has been reported that the lithium-based conversion layer growth period can be divided into five stages [32,51]. Up to 700 s after exposure, AA2024-T3 surface, except the S-phase does not show passivation (Stages I and II). Supersaturation of aluminate ions is realized at Stage III and the conversion layer then appears at the alloy surface. Stages IV and V correspond to the growth of the conversion layer and formation of the dense-like inner layer. The SECM results discussed above include the first two stages, where the alloy surface transits from an imperfect passive state to an active state and then gradually shifts back to a passive state. Initially, the alloy surface only undergoes a dissolution process, leading to the accumulation and supersaturation of aluminate ions which is the prerequisite for triggering the formation of the lithium-based conversion layer [24,51]. The S-, θ- and constituent phases act as active cathodic areas, but their potential differences compared to the potential of the aluminium matrix continue to change during the conversion layer formation process. Fig. 7 shows the SEI images of the alloy surface with different immersion treatments and corresponding SECM approach curves over the aluminium matrix. The results of the approach curves shown in Fig. 7e are consistent with the results of the surface reactivity variation through SECM mapping as presented before. The aluminium matrix without any conversion treatment still indicates substrate conductivity to some extent, indicating that the native aluminium oxide film contains compositional, structural and electronic defects, effectively enabling electrochemical activity

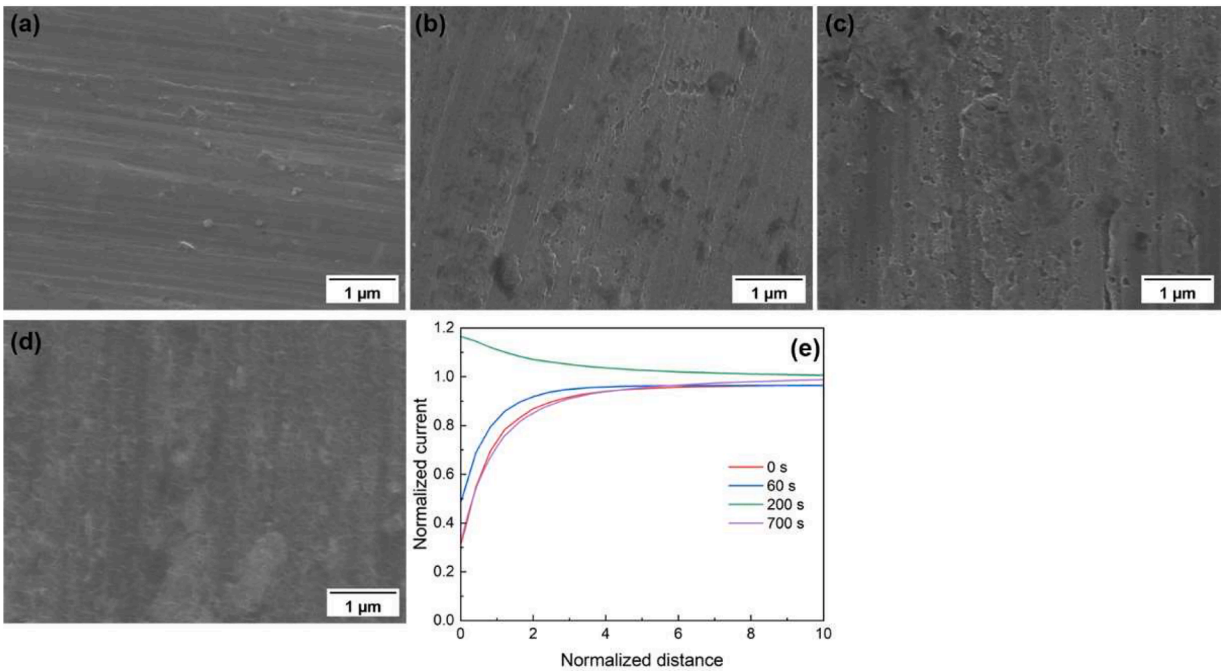

Fig. 7. SEM images for samples with a conversion treatment for 0 s (a), 60 s (b), 200 s (c), and 700 s (d), and SECM approach curves over the conversion layer corresponding to different immersion times in a borate butter solution containing 2 mM FcMeOH (e).

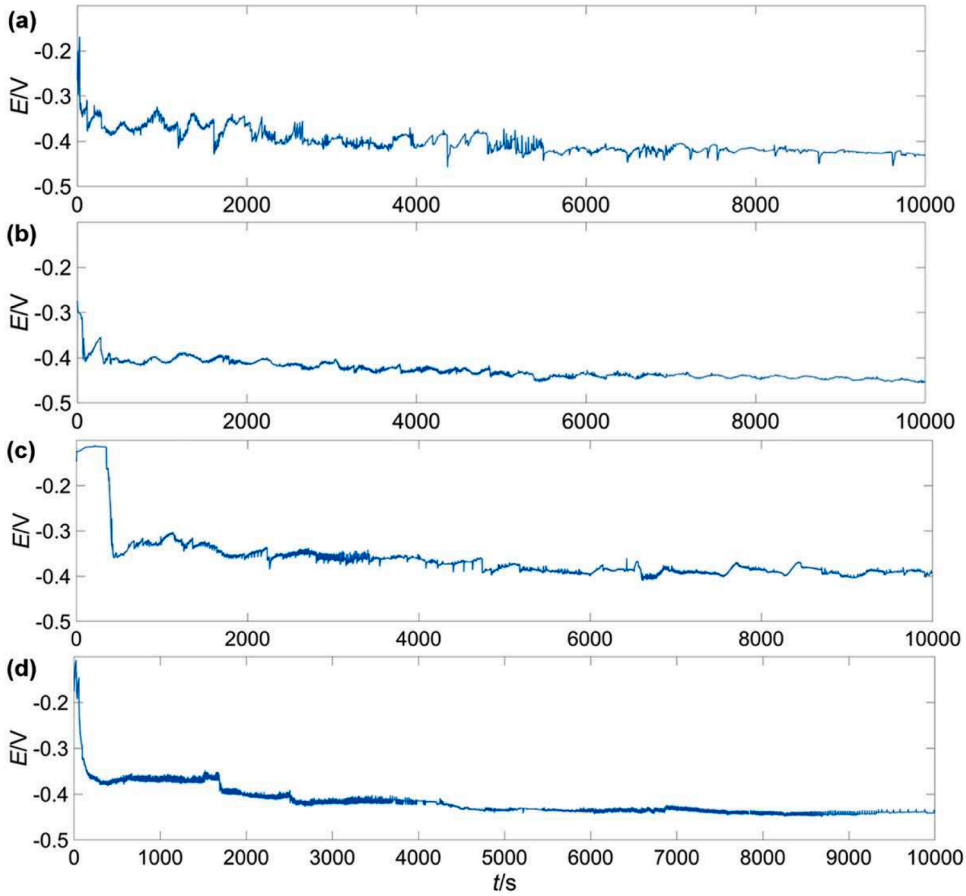

Fig. 8. EN potential signals for AA2024-T3 initially treated in 0.01 M NaCl and 0.01 M Li_2CO_3 solution for (a) 0 s, (b) 60 s, (c) 200 s, and (d) 700 s, and then exposed in a borate butter solution containing 2 mM FcMeOH for a duration of 10,000 s.

occurring at its surface. With the dissolution of the oxide layer in the conversion bath, surface conductivity increases and reaches its highest level at 200 s. This is confirmed by the different behaviour of the approach curves. For 0 and 60 s, curves show negative feedback response (normalized current < 1), while for 200 s condition, the curve shifts to positive feedback (normalized current > 1), indicating an electroactive behaviour of the surface. At 700 s, the curve shows again non-electroactive response (negative feedback) associated with a more insulating surface.

3.2. EN analysis

EN potential signals are recorded for samples immersed for four different durations in the lithium-based conversion bath at early stages to better support the explanations for the variations of SECM mapping. After recording the EN raw data, an eight-level DWT trend removal was applied to extract the part of the signal that contains corrosion information. Subsequently, EDP analysis was performed to reveal the dominant timescales in these EN potential signals [48,49]. Fig. 8 presents the samples initially immersed in the conversion solution for different times (0, 60, 200, 700 s) and then exposed to a borate buffer solution containing 2 mM FcMeOH. The potential noise evolution provides an indication of the surface activity and a lower potential usually indicates a more active surface state. It is clear that the potential signal firstly endures a small drop from 0 s (Fig. 8a) to 60 s formation condition (Fig. 8b) which is caused by the dissolution of the air-formed oxide layer [32].

Later, with the Cu enrichment over the aluminium matrix and IMPs [51], the potential value gradually rises (Fig. 8c). The slight potential decrease shown in Fig. 8d might attribute to the presence of hydrogen bubble-covered area which is more active compared to the uncovered region. A detailed discussion of the effect of attached hydrogen bubbles will be presented later. Time-frequency analysis can be considered as a suitable strategy to distinguish the local and uniform nature of electrochemical reactions [50]. Therefore, in this work time-frequency analysis is employed to investigate the nature of the potential differences and hence the nature of local galvanic interactions between the aluminium matrix and IMPs. A larger local IMP-matrix potential difference usually generates an EN signal where localized electrochemical reactions are more dominant in energy contribution. In other words, dominant energy bands are more likely to be manifested at a higher frequency domain. Fig. 9 shows the EDPs of samples with different conversion treatment times. D2 and D3 represent activation-controlled processes while D7 and D8 are related to more diffusion-controlled processes [50]. The sample without conversion treatment (Fig. 9a) shows the highest energy contribution in D7 and D8. This is probably due to the presence of the native oxide layer. For samples treated in the conversion bath for 60 s (Fig. 9b), D2 and D3 become larger and a marked decrease of D7 and D8 is visible. When the immersion time is extended to 200 s (Fig. 9c), the EDP shifts back to an energy distribution similar to that of Fig. 9a. This is in agreement with the results shown in Fig. 5, where SECM mapping presents a homogeneous current distribution. Finally, the alloy surface retains a more heterogenous potential distribution with a longer immersion time of 700 s (Fig. 9d). This is visible in the EDP as a relative increase of D2 and D3 again.

3.3. Late stages of the conversion layer formation

Three time points are chosen to represent the last three stages of the conversion layer formation process: 2000, 4000, and 14,500 s. Fig. 10 shows the SECM mapping and the corresponding BEI/EDX results for the specimen with a conversion layer formation time of 2000 s. It is observed that the averaged current continues to decline and that the potential difference between the IMPs and the aluminium matrix drops as well. Another finding is that not all types of IMPs act as active cathodes and that three active locations, marked in Fig. 10, are all related to the local presence of S-phase particles. The elemental composition of these three active zones is listed in Fig. S4. The potential differences between the aluminium matrix and the θ- or constituent phases are almost negligible. S-phase particles serving as active sites indicate that the potential of the S-phase is still higher than that of the surrounding aluminium matrix. This is possibly related to the more severe dealloying as compared to that of θ- and constituent phases, since the S-phase is a relatively active IMP [6,37,53]. A more pronounced dealloying leads to a larger extent of surface enrichment of Cu and a limited surface area coverage by the columnar outer layer which is not the dominant barrier

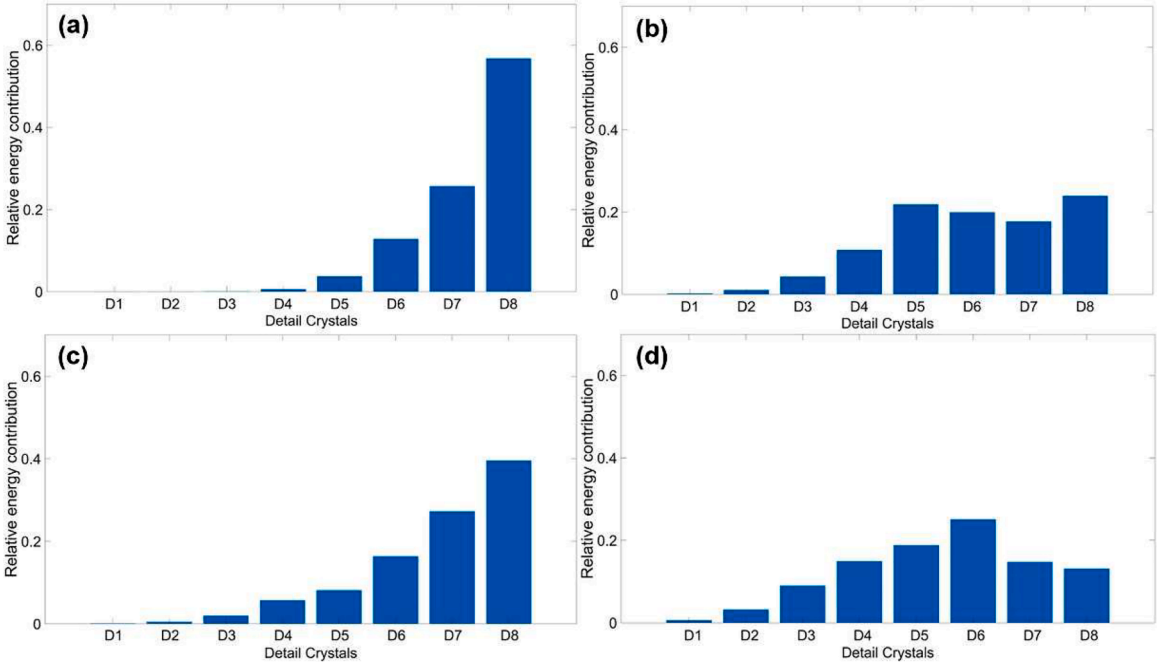

Fig. 9. Energy distribution plots of the EN current signals for AA2024-T3 immersed in 0.01 M NaCl and 0.01 M Li_2CO_3 solution for (a) 0 s, (b) 60 s, (c) 200 s, and (d) 700 s, and then exposed in a borate butter solution containing 2 mM FcMeOH. Timeframes are between 4000 s to 6000 s.

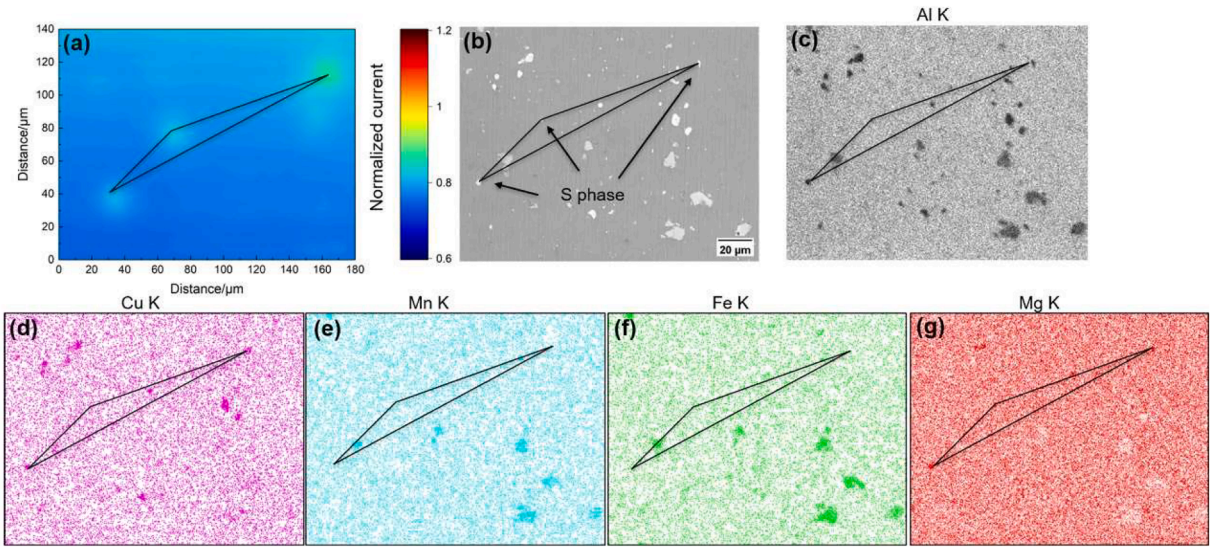

Fig. 10. SECM map of AA2024-T3 immersed in the conversion bath for 2000 s obtained at borate buffer solution containing 2 mM FcMeOH (a) and corresponding BEI image (b), and EDX maps for Al (c), Cu (d), Mn (e), Fe (f), Mg (g).

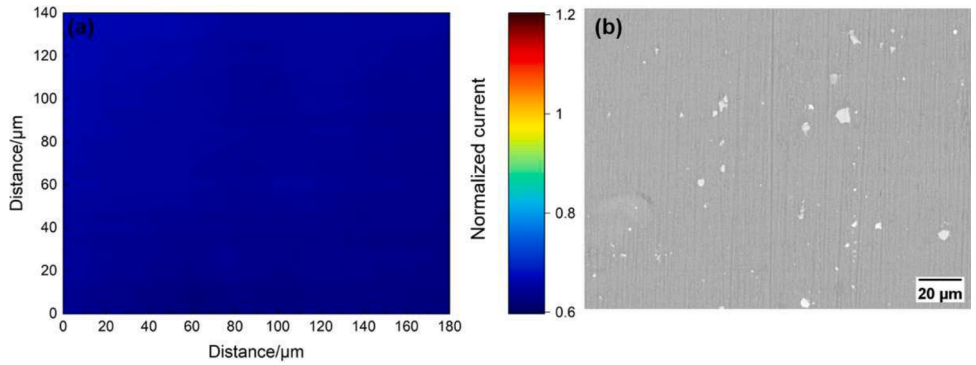

Fig. 11. SECM maps of AA2024-T3 immersed in the conversion bath for 4000 s obtained at borate buffer solution containing 2 mM FcMeOH (a) and corresponding BEI image (b).

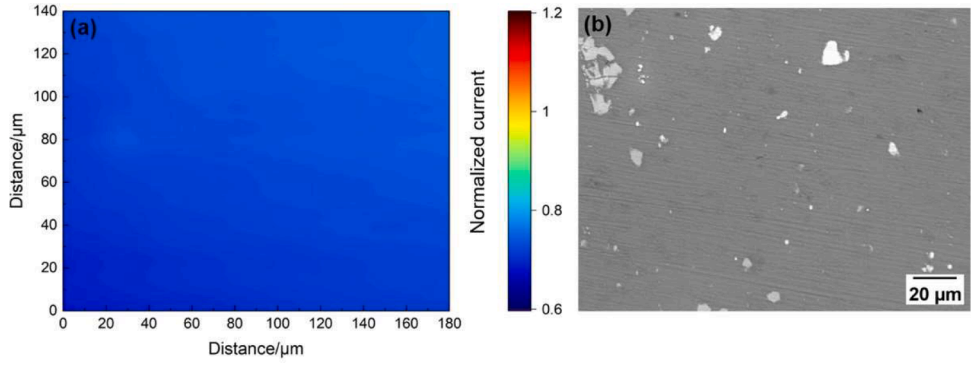

Fig. 12. SECM maps of AA2024-T3 immersed in the conversion bath for 14,500 s obtained at borate buffer solution containing 2 mM FcMeOH (a) and corresponding BEI image (b).

for corrosion protection [28] is insufficient to supress electrochemical reactions.

Figs. 11 and 12 show the SECM mapping and the corresponding BEI images for a duration of a lithium-based conversion treatment for 4000 s and 14,500 s, respectively. Their EDX results are shown in Fig. S5 and Fig. S6, respectively. After a longer exposure time, the alloy surface exhibits a homogeneous electrochemical behaviour; the potential difference between all three types of IMPs and the aluminium matrix has now become insignificant. This implies that the lithium-based conversion layer finally reaches a relatively intact and protective state, in which it inhibits electron exchange reactions at the substrate surface. Although it was previously reported that the dense inner layer provides the highest corrosion protection of all sublayers and that the formation of this inner layer is limited over the locations of IMPs [51], the formed

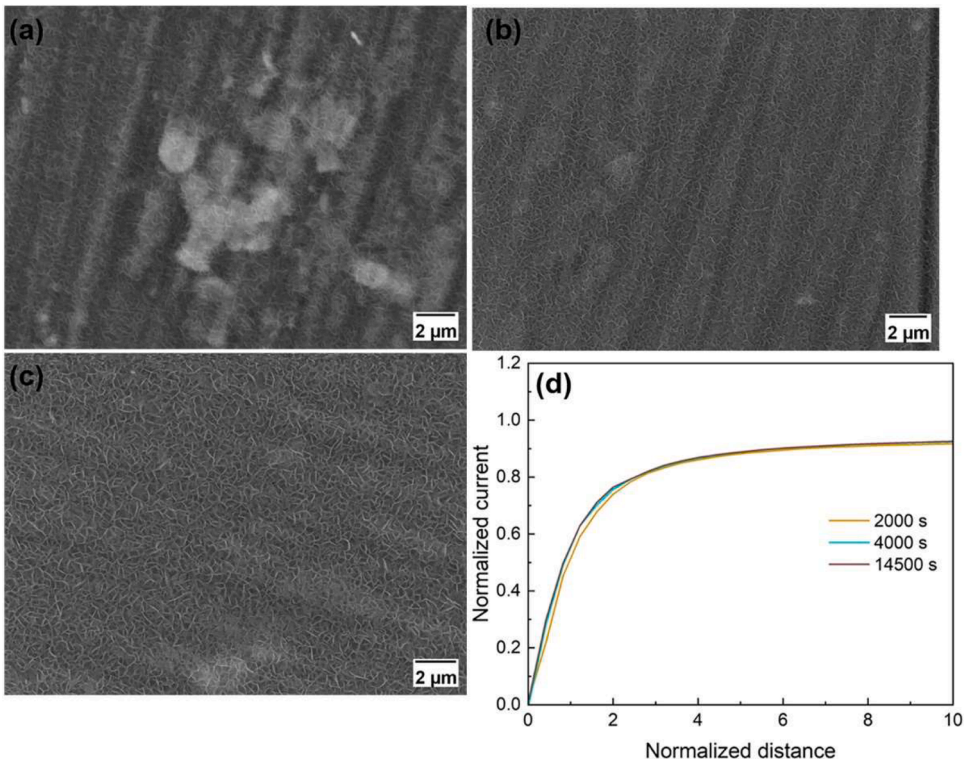

Fig. 13. SEM images for samples with a conversion treatment for 2000 s (a), 4000 s (b), and 14,500 s (c), and probe approach curves over the conversion layer correspondingly in a borate butter solution containing 2 mM FcMeOH (d).

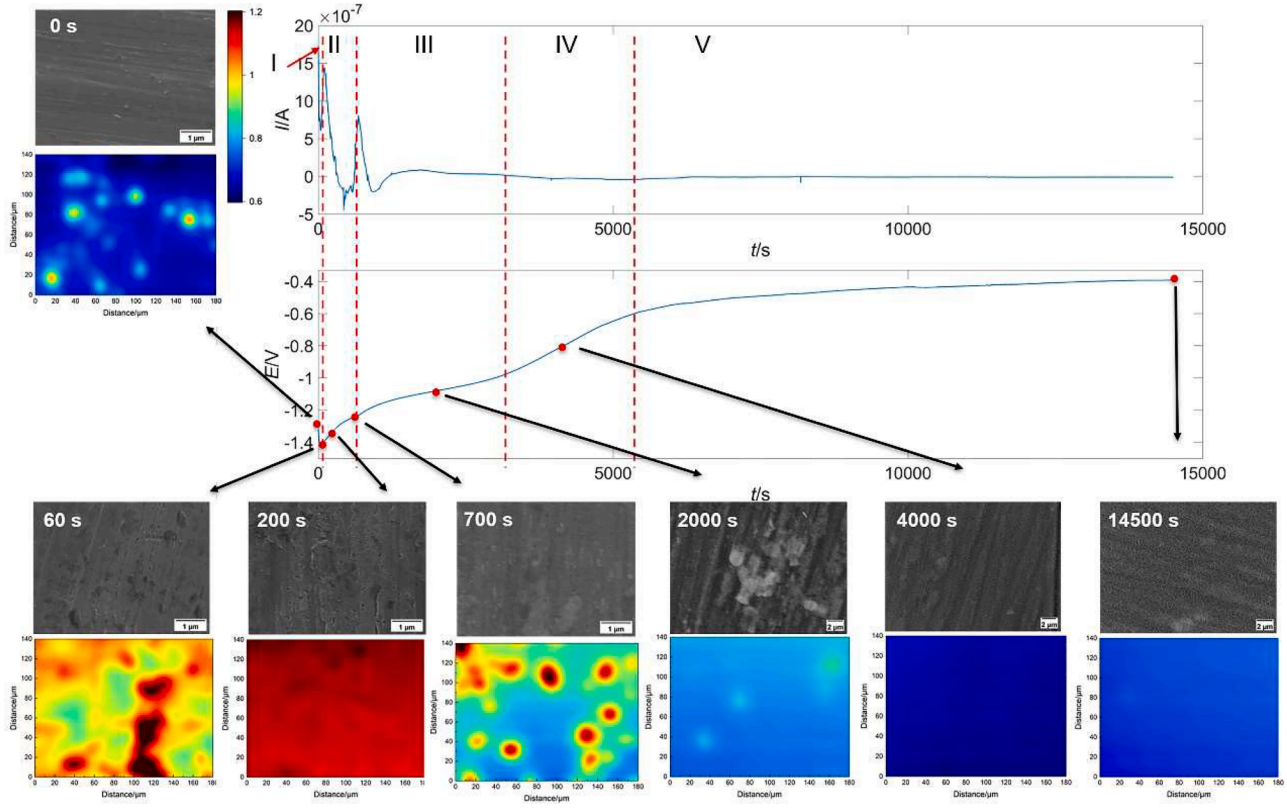

Fig. 14. Integral EN, SEM and SECM characterization results of the different stages of the formation process of a lithium-based conversion layer immersed in a 0.01 M NaCl and 0.01 M Li_2CO_3 solution for a duration of 14,500 s. The round red markers indicate seven selected time points for analysis. The EN data originates from our prior work [32].

layer effectively suppresses electrochemical activity in this case.

Fig. 13 shows the SEI images of the alloy surface with different immersion treatments during the last three stages and the corresponding approach curve over the aluminium matrix. The top columnar layer continues to grow at a relatively low speed for longer immersion times. The conversion layer, formed for a duration of at least 2000s, shows a passive behaviour since the normalized tip current almost reaches zero when the tip virtually contacts the alloy surface. This indicates that the size of the top columnar structure reaches the required dimensions to hinder electrochemical reactions occurring on the alloy surface.

Finally, SECM mapping and morphological observations can be linked to the EN measurement of the formation process of the lithium-based conversion layer which was reported previously [32]. As shown in Fig. 14, early stages I and II represent a rapidly changing system; the potential difference between the aluminium matrix and IMPs varies considerably, generating large amounts of current transients simultaneously [32]. Later, from stage III onwards, the potential difference gradually decreases and finally becomes negligible. Correspondingly, both the intensity and the number of current transients gradually diminish as well.

3.4. The effect of hydrogen evolution on the protectiveness of the conversion layer

Previous work has revealed that hydrogen bubbles generated from hydrogen evolution during the conversion layer formation attach to the alloy surface, although some detach from the specimen surface spontaneously [32]. Hydrogen bubbles locally isolate the alloy surface from the conversion bath solution and interrupt the growth of the lithium-based conversion layer. Therefore, a less well-developed conversion layer is formed at these locations, which is detrimental to the local corrosion protective properties. Fig. 15 shows an SECM normalized current map over a bubble-covered area after a lithium-based conversion bath for a duration of 14,500 s and matching SEI images. The bubble-covered area can be easily observed before adding the electrolyte to the SECM cell due to apparent colour differences (silvery white in round outline). Clearly, the bubble-covered area shows a higher local electrochemical activity, which indicates that the passivation of this area is less effective. Fig. 15b presents the morphological characterization and the bubble-covered area is marked by a red dashed line. The enlarged image of the edge bubble-covered area marked by the orange arrow is shown in Fig. 15c and central area indicated by the blue arrow in Fig. 15b is presented in Fig. 15d. The results show that the size of the petal-like structure of the columnar layer gradually shrinks in the direction toward the central bubble-occupied area (Fig. 15c). This indicates that the growth of the conversion layer stops at middle stages. As shown in Fig. 15d, the morphology in the central bubble-covered area is comparable to that of samples after a conversion bath for 700 s whose approach curve still indicates local surface activity, therefore manifesting insufficient passivation [28].

4. Conclusion

The local electrochemical behaviour of the alloy surface at and around IMPs at different stages of the formation process of the conversion layer at micrometre level was studied with SECM. At early stages (Stage I and II), the alloy surface does not show passivation but presents a rapidly changing characteristic. This largely dynamic system originates from the varying electrochemical potential differences at IMPs and that between the aluminium matrix and IMPs. At the last three stages (III to V), the potential difference gradually diminishes and finally the entire surface is passivated. During the conversion layer evolution process, the alloy surface experiences a transition from insufficient passivation to activation and then back to passivation. In the beginning, S-, θ- and constituent phases all act as active cathodic sites, and the passivation process of θ- and constituent phases precedes that of the S phase due to their higher electrochemical stability. The differences in electrochemical properties at the IMPs and between the aluminium matrix and IMPs lead to the formation of distinct structures of the protective layers covering the aluminium matrix and the IMPs. The evaluation of their

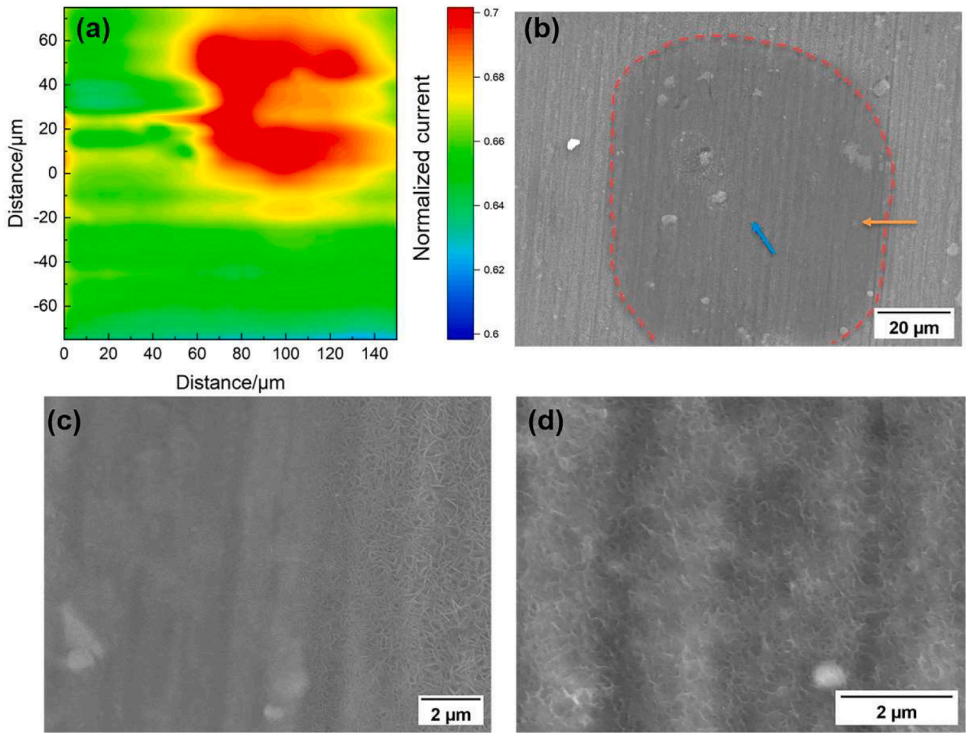

Fig. 15. SECM maps for a bubble-covered area of AA 2024-T3 immersed in the conversion bath for 14,500 s obtained at borate buffer solution containing 2 mM FcMeOH (a) and corresponding SEM images (b), the zoomed-in image in Fig. 15 (b) along the orange arrow (c), and the zoomed-in image in Fig. 15 (b) indicated by the blue arrow (d).

protectiveness against corrosion over time requires further study. As a final remark, hydrogen bubbles are shown to be detrimental to the growth of the conversion layer in case these attach to the alloy surface at the early stages of the conversion process.

CRediT authorship contribution statement

Ziyu Li: Project administration, Investigation, Formal analysis, Writing – original draft. **Gaojie Li:** Writing – review & editing. **Peter Visser:** Writing – review & editing. **Axel Homborg:** Conceptualization, Supervision, Writing – review & editing. **Yaiza Gonzalez-Garcia:** Conceptualization, Supervision, Writing – review & editing. **Arjan Mol:** Conceptualization, Supervision, Writing – review & editing.

Declaration of Competing Interest

The authors declare that they have no known competing financial interests or personal relationships that could have appeared to influence the work reported in this paper.

Data availability

Data will be made available on request.

Acknowledgment

The authors wish to acknowledge the financial support from the China Scholarship Council (CSC).

Supplementary materials

Supplementary material associated with this article can be found, in the online version, at doi:10.1016/j.electacta.2023.143270.

References

[1] N.L. Sukiman, X. Zhou, N. Birbilis, A.E. Hughes, J.M.C. Mol, S. J, X. Zhou, E. G, Durability and corrosion of aluminium and its alloys: overview, property space, techniques and developments, in: Z. Ahmad (Ed.), Aluminium Alloys - New Trends in Fabrication and Applications, InTech, 2012, https://doi.org/10.5772/53752.
[2] A. E, N. Birbilis, M.C. J, J. S, X. Zhou, E. G, High strength al-alloys: microstructure, corrosion and principles of protection, in: Z. Ahmad (Ed.), Recent Trends in Processing and Degradation of Aluminium Alloys, InTech, 2011, https://doi.org/10.5772/18766.
[3] A.E. Hughes, C. MacRae, N. Wilson, A. Torpy, T.H. Muster, A.M. Glenn, Sheet AA2024-T3: a new investigation of microstructure and composition, Surf. Interface Anal 42 (2010) 334–338, https://doi.org/10.1002/sia.3163.
[4] A. Boag, A.E. Hughes, N.C. Wilson, A. Torpy, C.M. MacRae, A.M. Glenn, T. H. Muster, How complex is the microstructure of AA2024-T3? Corros. Sci. 51 (2009) 1565–1568, https://doi.org/10.1016/j.corsci.2009.05.001.
[5] N. Birbilis, Y.M. Zhu, S.K. Kairy, M.A. Glenn, J.F. Nie, A.J. Morton, Y. Gonzalez-Garcia, H. Terryn, J.M.C. Mol, A.E. Hughes, A closer look at constituent induced localised corrosion in Al-Cu-Mg alloys, Corros. Sci. 113 (2016) 160–171, https://doi.org/10.1016/j.corsci.2016.10.018.
[6] A. Kosari, F. Tichelaar, P. Visser, H. Zandbergen, H. Terryn, J.M.C. Mol, Dealloying-driven local corrosion by intermetallic constituent particles and dispersoids in aerospace aluminium alloys, Corros. Sci. 177 (2020), 108947, https://doi.org/10.1016/j.corsci.2020.108947.
[7] P. Visser, H. Terryn, J.M.C. Mol, Aerospace coatings, in: A.E. Hughes, J.M.C. Mol, M.L. Zheludkevich, R.G. Buchheit (Eds.), Aerospace coatings, Active Protective Coatings: New-Generation Coatings for Metals (2016) 315–372, https://doi.org/10.1007/978-94-017-7540-3_12.
[8] A.E. Hughes, J.M.C. Mol, M.L. Zheludkevich, R.G. Buchheit (Eds.), Active Protective Coatings: New-Generation Coatings For Metals, Springer Netherlands, Dordrecht, 2016, https://doi.org/10.1007/978-94-017-7540-3.
[9] R.G. Buchheit, R.K. Boger, M.C. Carroll, R.M. Leard, C. Paglia, J.L. Searles, The electrochemistry of intermetallic particles and localized corrosion in Al alloys, JOM 53 (2001) 29–33, https://doi.org/10.1007/s11837-001-0084-x.
[10] N. Birbilis, R.G. Buchheit, Electrochemical characteristics of intermetallic phases in aluminum alloys: an experimental survey and discussion, J. Electrochem. Soc. 152 (2005) B140, https://doi.org/10.1149/1.1869984.
[11] I. Milošev, G.S. Frankel, Review—conversion coatings based on zirconium and/or titanium, J. Electrochem. Soc. 165 (2018) C127, https://doi.org/10.1149/2.0371803jes.
[12] M. Becker, Chromate-free chemical conversion coatings for aluminum alloys, Corros. Rev. 37 (2019) 321–342, https://doi.org/10.1515/corrrev-2019-0032.
[13] P.S. Coloma, U. Izagirre, Y. Belaustegi, J.B. Jorcin, F.J. Cano, N. Lapeña, Chromium-free conversion coatings based on inorganic salts (Zr/Ti/Mn/Mo) for aluminum alloys used in aircraft applications, Appl. Surf. Sci. 345 (2015) 24–35, https://doi.org/10.1016/j.apsusc.2015.02.179.
[14] P. Visser, S.A. Hayes, Anti-Corrosive Coating Composition, WIP Organ, 2010, p. A1. Ed WO. 112605.
[15] P. Visser, H. Terryn, J.M.C. Mol, Active corrosion protection of various aluminium alloys by lithium-leaching coatings, Surf. Interface Anal. 51 (2019) 1276–1287, https://doi.org/10.1002/sia.6638.
[16] P. Visser, Y. Liu, X. Zhou, T. Hashimoto, G.E. Thompson, S.B. Lyon, L.G.J. van der Ven, A.J.M.C. Mol, H.A. Terryn, The corrosion protection of AA2024-T3 aluminium alloy by leaching of lithium-containing salts from organic coatings, Faraday Discuss 180 (2015) 511–526, https://doi.org/10.1039/C4FD00237G.
[17] P. Visser, H. Terryn, J.M.C. Mol, On the importance of irreversibility of corrosion inhibitors for active coating protection of AA2024-T3, Corros. Sci. 140 (2018) 272–285, https://doi.org/10.1016/j.corsci.2018.05.037.
[18] J. Gui, T.M. Devine, Influence of lithium on the corrosion of aluminum, Scr. Met. U. S. 21 (1987) 6, https://doi.org/10.1016/0036-9748(87)90336-X.
[19] C.M. Rangel, M.A. Travassos, The passivation of aluminium in lithium carbonate/bicarbonate solutions, Corros. Sci. 33 (1992) 327–343, https://doi.org/10.1016/0010-938X(92)90064-A.
[20] C.M. Rangel, M.A. Travassos, Li-based conversion coatings on aluminium: an electrochemical study of coating formation and growth, Surf. Coat. Technol. 200 (2006) 5823–5828, https://doi.org/10.1016/j.surfcoat.2005.08.145.
[21] G.R. Williams, D. O'Hare, A kinetic study of the intercalation of lithium salts into Al(OH)3, J. Phys. Chem. B 110 (2006) 10619–10629, https://doi.org/10.1021/jp057130k.
[22] C.A. Drewien, M.O. Eatough, D.R. Tallant, C.R. Hills, R.G. Buchheit, Lithium-aluminum-carbonate-hydroxide hydrate coatings on aluminum alloys: composition, structure, and processing bath chemistry, J. Mater. Res. 11 (1996) 1507–1513, https://doi.org/10.1557/JMR.1996.0188.
[23] R.G. Buchheit, M.D. Bode, G.E. Stoner, Corrosion-resistant, chromate-free talc coatings for aluminum, Corrosion 50 (1994) 205–214, https://doi.org/10.5006/1.3293512.
[24] P. Visser, A. Lutz, J.M.C. Mol, H. Terryn, Study of the formation of a protective layer in a defect from lithium-leaching organic coatings, Prog. Org. Coat. 99 (2016) 80–90, https://doi.org/10.1016/j.porgcoat.2016.04.028.
[25] K. Marcoen, P. Visser, G.F. Trindade, M.L. Abel, J.F. Watts, J.M.C. Mol, H. Terryn, T. Hauffman, Compositional study of a corrosion protective layer formed by leachable lithium salts in a coating defect on AA2024-T3 aluminium alloys, Prog. Org. Coat. 119 (2018) 65–75, https://doi.org/10.1016/j.porgcoat.2018.02.011.
[26] M. Meeusen, P. Visser, L. Fernández Macía, A. Hubin, H. Terryn, J.M.C. Mol, The use of odd random phase electrochemical impedance spectroscopy to study lithium-based corrosion inhibition by active protective coatings, Electrochim. Acta 278 (2018) 363–373, https://doi.org/10.1016/j.electacta.2018.05.036.
[27] J.S. Laird, P. Visser, S. Ranade, A.E. Hughes, H. Terryn, J.M.C. Mol, Li leaching from lithium carbonate-primer: an emerging perspective of transport pathway development, Prog. Org. Coat. 134 (2019) 103–118, https://doi.org/10.1016/j.porgcoat.2019.04.062.
[28] P. Visser, Y. Gonzalez-Garcia, J.M.C. Mol, H. Terryn, Mechanism of passive layer formation on AA2024-T3 from alkaline lithium carbonate solutions in the presence of sodium chloride, J. Electrochem. Soc. 165 (2018) C60–C70, https://doi.org/10.1149/2.1011802jes.
[29] A. Kosari, P. Visser, F. Tichelaar, S. Eswara, J.N. Audinot, T. Wirtz, H. Zandbergen, H. Terryn, J.M.C. Mol, Cross-sectional characterization of the conversion layer formed on AA2024-T3 by a lithium-leaching coating, Appl. Surf. Sci. 512 (2020), 145665, https://doi.org/10.1016/j.apsusc.2020.145665.
[30] P. Visser, M. Meeusen, Y. Gonzalez-Garcia, H. Terryn, J.M.C. Mol, Electrochemical evaluation of corrosion inhibiting layers formed in a defect from lithium-leaching organic coatings, J. Electrochem. Soc. 164 (2017) C396–C406, https://doi.org/10.1149/2.1411707jes.
[31] Y. Liu, P. Visser, X. Zhou, S.B. Lyon, T. Hashimoto, M. Curioni, A. Gholinia, G. E. Thompson, G. Smyth, S.R. Gibbon, D. Graham, J.M.C. Mol, H. Terryn, Protective film formation on AA2024-T3 aluminum alloy by leaching of lithium carbonate from an organic coating, J. Electrochem. Soc. 163 (2015) C45, https://doi.org/10.1149/2.0021603jes.
[32] Z. Li, A. Homborg, Y. Gonzalez-Garcia, A. Kosari, P. Visser, A. Mol, Evaluation of the formation and protectiveness of a lithium-based conversion layer using electrochemical noise, Electrochim. Acta 426 (2022), 140733, https://doi.org/10.1016/j.electacta.2022.140733.
[33] Z. Li, A. Homborg, Y. Gonzalez-Garcia, P. Visser, M. Soleimani, A. Mol, The effect of ambient ageing on the corrosion protective properties of a lithium-based conversion layer, J. Electrochem. Soc. 170 (2023), 031504, https://doi.org/10.1149/1945-7111/acc1a6.
[34] A. Boag, A.E. Hughes, A.M. Glenn, T.H. Muster, D. McCulloch, Corrosion of AA2024-T3 part I: localised corrosion of isolated IM particles, Corros. Sci. 53 (2011) 17–26, https://doi.org/10.1016/j.corsci.2010.09.009.
[35] A.E. Hughes, A. Boag, A.M. Glenn, D. McCulloch, T.H. Muster, C. Ryan, C. Luo, X. Zhou, G.E. Thompson, Corrosion of AA2024-T3 part II: co-operative corrosion, Corros. Sci. 53 (2011) 27–39, https://doi.org/10.1016/j.corsci.2010.09.030.
[36] A.M. Glenn, T.H. Muster, C. Luo, X. Zhou, G.E. Thompson, A. Boag, A.E. Hughes, Corrosion of AA2024-T3 part III: propagation, Corros. Sci. 53 (2011) 40–50, https://doi.org/10.1016/j.corsci.2010.09.035.

[37] A. Kosari, H. Zandbergen, F. Tichelaar, P. Visser, P. Taheri, H. Terryn, J.M.C. Mol, In-situ nanoscopic observations of dealloying-driven local corrosion from surface initiation to in-depth propagation, Corros. Sci. 177 (2020), 108912, https://doi.org/10.1016/j.corsci.2020.108912.
[38] D. Polcari, P. Dauphin-Ducharme, J. Mauzeroll, Scanning electrochemical microscopy: a comprehensive review of experimental parameters from 1989 to 2015, Chem. Rev. 116 (2016) 13234–13278, https://doi.org/10.1021/acs.chemrev.6b00067.
[39] A. Singh, Y. Lin, W. Liu, S. Yu, J. Pan, C. Ren, D. Kuanhai, Plant derived cationic dye as an effective corrosion inhibitor for 7075 aluminum alloy in 3.5% NaCl solution, J. Ind. Eng. Chem. 20 (2014) 4276–4285, https://doi.org/10.1016/j.jiec.2014.01.033.
[40] M.B. Jensen, A. Guerard, D.E. Tallman, G.P. Bierwagen, Studies of electron transfer at aluminum alloy surfaces by scanning electrochemical microscopy, J. Electrochem. Soc. 155 (2008) C324, https://doi.org/10.1149/1.2916734.
[41] J.C. Seegmiller, D.A. Buttry, A SECM study of heterogeneous redox activity at AA2024 surfaces, J. Electrochem. Soc. 150 (2003) B413, https://doi.org/10.1149/1.1593041.
[42] V. Upadhyay, D. Battocchi, Localized electrochemical characterization of organic coatings: a brief review, Prog. Org. Coat. 99 (2016) 365–377, https://doi.org/10.1016/j.porgcoat.2016.06.012.
[43] M.B. Jensen, M.J. Peterson, N. Jadhav, V.J. Gelling, SECM investigation of corrosion inhibition by tungstate- and vanadate-doped polypyrrole/aluminum flake composite coatings on AA2024-T3, Prog. Org. Coat. 77 (2014) 2116–2122, https://doi.org/10.1016/j.porgcoat.2014.05.019.
[44] L. Niu, Y. Yin, W. Guo, M. Lu, R. Qin, S. Chen, Application of scanning electrochemical microscope in the study of corrosion of metals, J. Mater. Sci. 44 (2009) 4511–4521, https://doi.org/10.1007/s10853-009-3654-x.
[45] H. Konno, S. Kobayashi, H. Takahashi, M. Nagayama, The hydration of barrier oxide films on aluminium and its inhibition by chromate and phosphate ions, Corros. Sci. 22 (1982) 913–923, https://doi.org/10.1016/0010-938X(82)90061-0.
[46] S. Guo, J.J. Leavitt, X. Zhou, E. Lahti, J. Zhang, Corrosion of aluminium alloy 1100 in post-LOCA solutions of a nuclear reactor, RSC Adv. 6 (2016) 44119–44128, https://doi.org/10.1039/C6RA07440E.
[47] S. Doulami, K. Beligiannis, Th. Dimogerontakis, V. Ninni, I. Tsangaraki-Kaplanoglou, The influence of some triphenylmethane compounds on the corrosion inhibition of aluminium, Corros. Sci. 46 (2004) 1765–1776, https://doi.org/10.1016/j.corsci.2003.10.014.
[48] A.M. Homborg, T. Tinga, X. Zhang, E.P.M. van Westing, P.J. Oonincx, J.H.W. de Wit, J.M.C. Mol, Time–frequency methods for trend removal in electrochemical noise data, Electrochim. Acta 70 (2012) 199–209, https://doi.org/10.1016/j.electacta.2012.03.062.
[49] Ł. Lentka, J. Smulko, Methods of trend removal in electrochemical noise data – overview, Measurement 131 (2019) 569–581, https://doi.org/10.1016/j.measurement.2018.08.023.
[50] A.M. Homborg, T. Tinga, E.P.M. van Westing, X. Zhang, G.M. Ferrari, J.H.W. de Wit, J.M.C. Mol, A critical appraisal of the interpretation of electrochemical noise for corrosion studies, Corrosion 70 (2014) 971–987, https://doi.org/10.5006/1277.
[51] A. Kosari, F. Tichelaar, P. Visser, H. Zandbergen, H. Terryn, J.M.C. Mol, Laterally-resolved formation mechanism of a lithium-based conversion layer at the matrix and intermetallic particles in aerospace aluminium alloys, Corros. Sci. 190 (2021), 109651, https://doi.org/10.1016/j.corsci.2021.109651.
[52] P. Cornette, S. Zanna, A. Seyeux, D. Costa, P. Marcus, The native oxide film on a model aluminium-copper alloy studied by XPS and ToF-SIMS, Corros. Sci. 174 (2020), 108837, https://doi.org/10.1016/j.corsci.2020.108837.
[53] A. Kosari, M. Ahmadi, F. Tichelaar, P. Visser, Y. Gonzalez-Garcia, H. Zandbergen, H. Terryn, J.M.C. Mol, Choice—dealloying-driven cerium precipitation on intermetallic particles in aerospace aluminium alloys, J. Electrochem. Soc 168 (2021), 041505, https://doi.org/10.1149/1945-7111/abf50d.